ELSEVIER

Volume 184, Issue 10, October 2011

JOURNAL OF SOLID STATE CHEMISTRY

www.elsevier.com/locate/jssc

CONTENTS

Abstracted/indexed in BioEngineering Abstracts, Chemical Abstracts, Coal Abstracts, Current Contents/Physics, Chemical, & Earth Sciences, Engineering Index, Research Alert, SCISEARCH, Science Abstracts, and Science Citation Index. Also covered in the abstract and citation database SCOPUS®. Full text available on ScienceDirect®.

Regular Articles

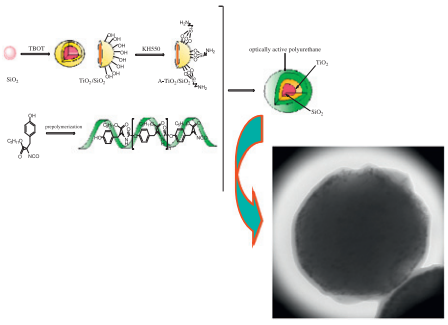

Optically active polyurethane/titania/silica (LPU/TiO_2/SiO_2) multilayered core–shell composite microspheres were prepared by the combination of titania deposition on the surface of silica spheres and subsequent polymer grafting.

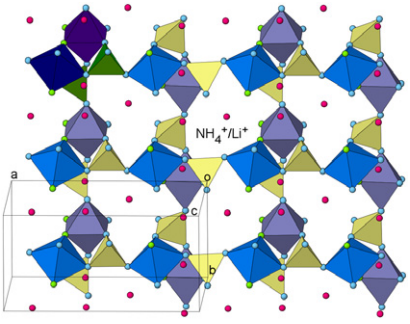

Three-dimensional structure of $(NH_4)_{0.80}Li_{0.20}[Fe(AsO_4)F]$, a fluoroarsenate containing lithium and ammonium in the structural cavities.

Regular Articles—Continued

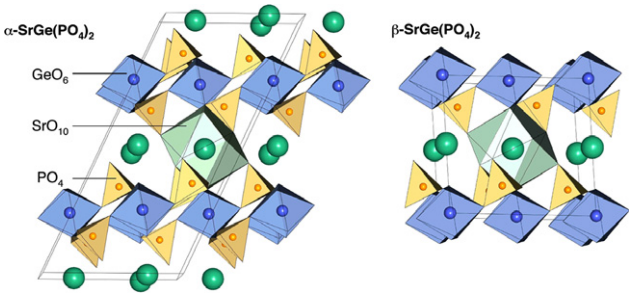

The superstructure of $SrGe(PO_4)_2$ at room temperature () results from the off-centering of cation Sr^{II}.

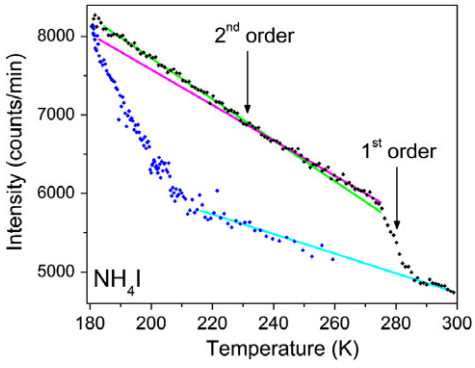

The transmission of very long wavelength neutrons is a highly sensitive probe of dynamical transitions in hydrogenous materials.

Continued

New phases in the system $LiMnVO_4$–$Mn_3(VO_4)_2$
Oliver Clemens, Robert Haberkorn and Horst Philipp Beck
page 2640

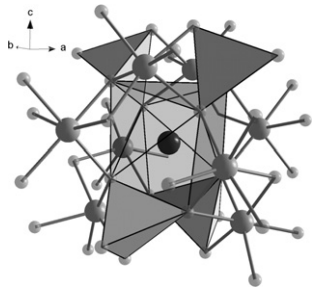

The unusual coordination of Mn in the form of a stella quadrangula with the surrounding vanadate groups.

Phase diagram, chemical stability and physical properties of the solid-solution $Ba_4Nb_{2-x}Ta_xO_9$
Matthew T. Dunstan, Peter D. Southon, Cameron J. Kepert, James Hester, Justin A. Kimpton and Chris D. Ling
page 2648

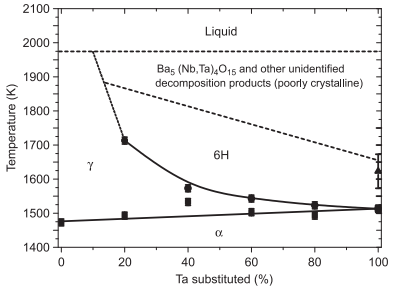

Thermodynamic phase diagram of $Ba_4Nb_{2-x}Ta_xO_9$.

Preparation and characterization of ordered porous carbons for increasing hydrogen storage behaviors
Seul-Yi Lee and Soo-Jin Park
page 2655

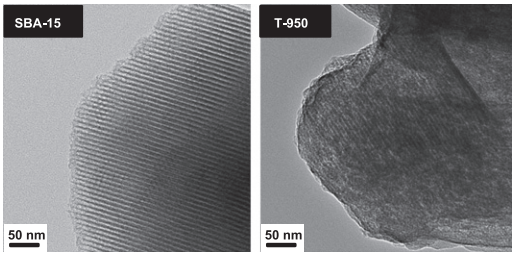

It is described that the considerable long-range ordering and the presence of mono-dimensional aligned channels between the two aligned nanorods of the porous framework from the SBA-15 was retained in the T-950 sample during the carbonization process.

Mid-infrared spectroscopic study of crystallization of cubic spinel phase from metakaolin
Petr Ptáček, František Šoukal, Tomáš Opravil, Magdaléna Nosková, Jaromír Havlica and Jiří Brandštetr
page 2661

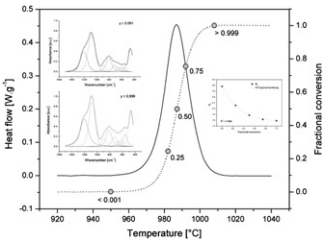

The thermal conversion of metakaolinite into spinel phase was investigated by mid-infrared spectroscopy to found relationship between bands features and fractional convesrion.

Decomposition of molybdate–hexamethylenetetramine complex: One single source route for different catalytic materials
Sandra Chouzier, Tivadar Czeri, Magalie Roy-Auberger, Christophe Pichon, Christophe Geantet, Michel Vrinat and Pavel Afanasiev
page 2668

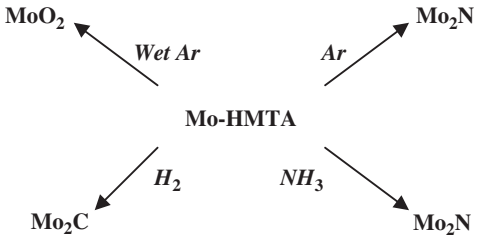

Depending on the conditions, decomposition of molybdate–HTMA complex yields highly dispersed molybdenum nitride, carbide or oxide.

Growth and characterization of Cl-doped ZnO hexagonal nanodisks
Ramin Yousefi, A.K. Zak and M.R. Mahmoudian
page 2678

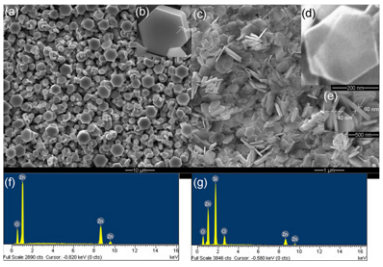

Cl-doped ZnO nanodisks and undoped ZnO microdisks have been grown using a thermal evaporation method.

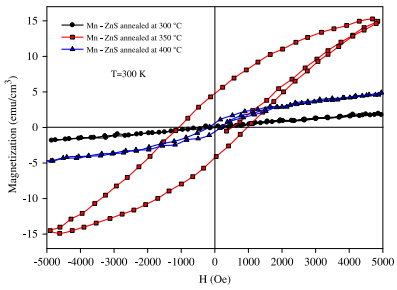

M–H variation of Mn diffusion-doped Zn(O,S) thin films measured at 300 K.

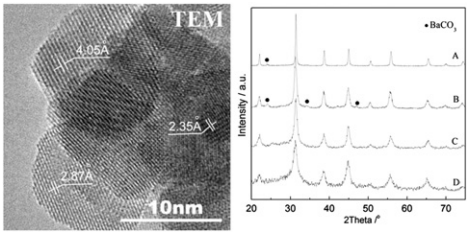

This paper offers a direct facile approach to $BaTiO_3$ nanoparticles at room temperature with a large quantity. The grain size can be modulated purposefully.

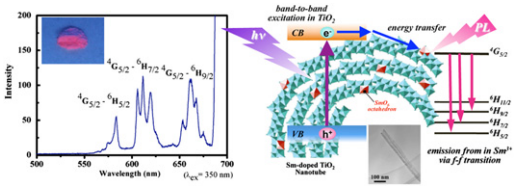

Samarium-doped TiO_2 nanotubes (TNTs) having a nanotubular structure were synthesized by soft chemical route. It was revealed that the energy associated by the band-to-band excitation of TNT matrix transferred to the doped Sm^{3+} ions in the lattice, resulting in emission of strong and visible red fluorescence.

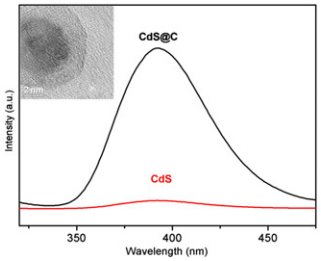

We demonstrated a facile approach to synthesize well-dispersed carbon-coated CdS quantum dots. The as-prepared nanoparticles presented remarkable fluorescence enhancement effect.

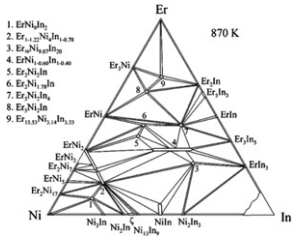

Phase relations in the ternary system Er–Ni–In have been established for the isothermal section at $T = 870$ K based on X-ray phase and EDX-analyses. Nine ternary compounds were observed.

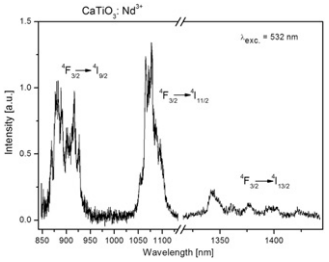

The 300 K emission spectrum of $CaTiO_3$: 1% Nd^{3+} annealed at 700 °C and measured at 300 K on InGaAs detector.

Continued

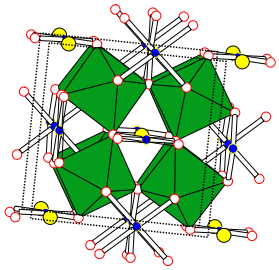

Structure of $CaCu_3Ru_4O_{12}$ showing the RuO_6 octahedra and the square planar environment for Cu^{2+}.

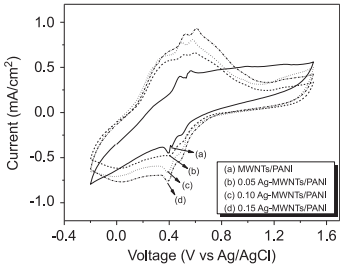

The current density of MWNTs/PANI increased with increasing the Ag concentration due to the bridge effect of Ag nanoparticles incorporated between MWNTs and PANI.

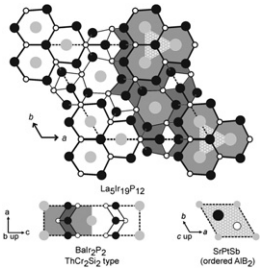

The intergrowth structure $La_5Ir_{19}P_{12}$.

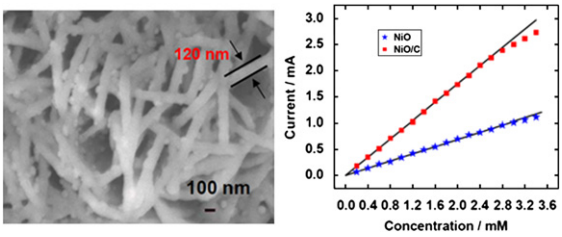

The thickness of nanosheets is about 90–120 nm. They are decorated with small particles. In glucose sensing, NiO and carbon composite exhibits higher response current than pure NiO.

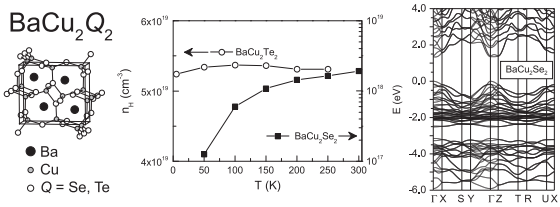

Combined experimental and theoretical study of orthorhombic $BaCu_2Se_2$ and $BaCu_2Te_2$ to assess potential for photovoltaic and thermoelectric applications.

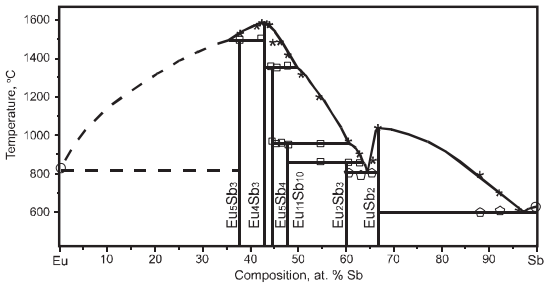

The high-temperature range of the T–x phase diagram for the Eu–Sb system.

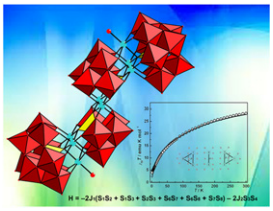

S-shaped multi-iron substituted arsenotungstate consisting of two asymmetric sandwich-type subunits has been hydrothermally synthesized and structurally characterized. Its magnetic properties have been investigated.

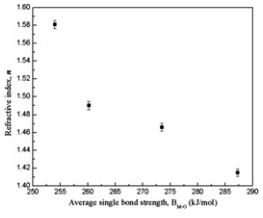

O1*s*, Yamashita–Kurosawa's parameter and average single bond strength of charge overlapping between electronic shells are used to explain enhanced oxide ion 2*p* electron density, which increases refractive index of glasses.

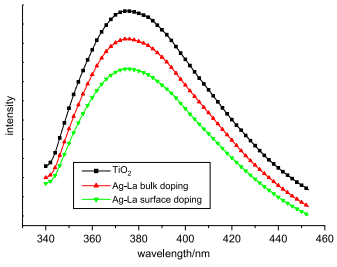

The PL intensity of Ag^{+} and La^{3+} surface codoped TiO_2 was the lowest among all samples, indicating the recombination of electron and hole was effectively prohibited compared with pure TiO_2, Ag^{+} and La^{3+} bulk codoped TiO_2.

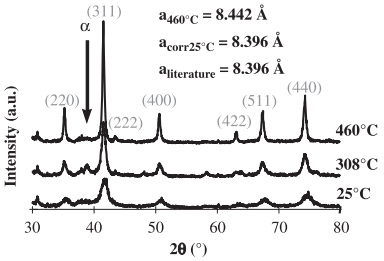

XRD patterns of $Fe_{3(1-\delta)}O_4$ nanometric powders obtained *in situ* during a reducing treatment. The stoichiometric compound was obtained by a thermal annealing at 460 °C under $pO_2 = 3 \times 10^{-26}$ Pa ($\Phi_{DRX} = 100$ nm). In inset, data of the experimental lattice parameter compared to the theoretical one. α represents the rhomboedrical phase which precipitates during this thermal treatment, then disappeared.

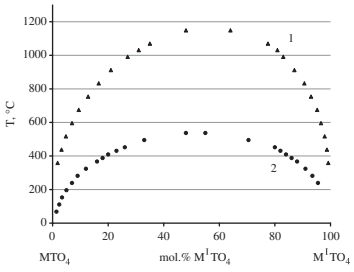

Calculated boundaries of solid solutions in $BaWO_4$–$CaWO_4$ (1) and $PbMoO_4$–$CaMoO_4$ (2) systems.

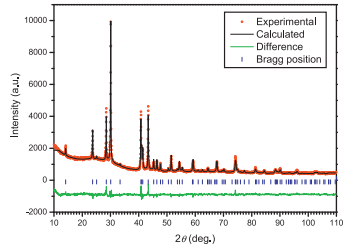

A new structure of the $R\bar{3}c$ space group with cell parameters of $a = 4.422(1)$ Å and $c = 37.524(3)$ Å was obtained from hydrothermal-grown $KBe_2BO_3F_2$ crystals by powder XRD and Rietveld refinement.

Continued

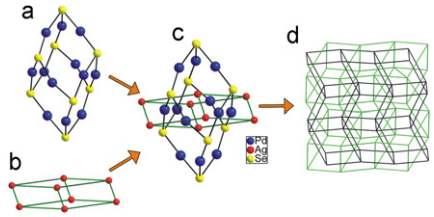

(a) Prolate rhombohedron formed by Pd and Se atoms, (b) oblate rhombohedron formed by Ag atoms and (c) their interpenetration at unit cell level. (d) 3D network of prolate and oblate rhombohedra.

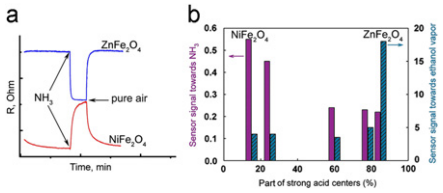

(a) *n*- and *p*-types change in electrical resistance and (b) sensor signal of $Ni_xZn_{1-x}Fe_2O_4$ towards NH_3 and ethanol vapor *vs.* the part of strong acid sites.

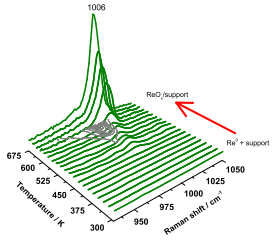

Evolution of the 900–1000 cm^{-1} region of the Raman spectrum of a mixture of metal rhenium with anatase TiO_2 K03 upon heating in pure O_2.

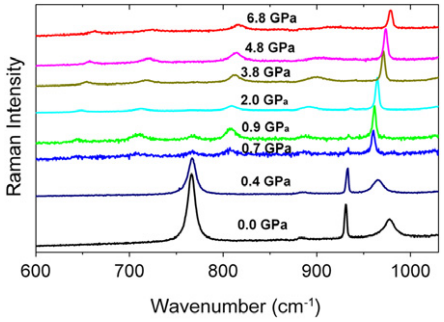

Raman spectra of $RbFe(MoO_4)_2$ crystal in the high wavenumber region recorded at different pressures during compression experiment.

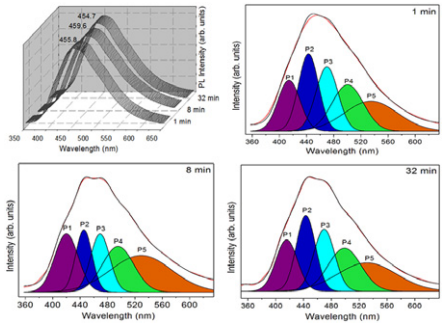

Nanostructural β-$Ni(OH)_2$ crystalline powders were prepared by rapid microwave–hydrothermal method for 1, 8 and 32 min. The hexagonal-shaped nanoplates obtained presented PL emission in the blue-green region and each decomposed component represents a different type of electronic transition, which can be linked to the structural arrangement or surface defects.